Earthworm coelomocyte internalization of MoS2 nanosheets: multiplexed imaging, molecular profiling, and computational modeling

Sun, K.; White, J.C.; He, E.; Gestel, C.A.M. van; Zhang, P.; Peijnenburg, W.J.G.M.; Qiu, H.

Environmental Science & Technology

pubs.acs.org/est

Article

Earthworm Coelomocyte Internalization of MoS_2 Nanosheets: Multiplexed Imaging, Molecular Profiling, and Computational Modeling

Kailun Sun, Jason C. White, Erkai He, Cornelis A. M. Van Gestel, Peng Zhang, Willie J.G.M. Peijnenburg, and Hao Qiu*

Cite This: *Environ. Sci. Technol.* 2023, 57, 21637−21649

Read Online

ACCESS | Metrics & More | Article Recommendations | Supporting Information

ABSTRACT: Fully understanding the cellular uptake and intracellular localization of MoS_2 nanosheets ($NSMoS_2$) is a prerequisite for their safe applications. Here, we characterized the uptake profile of $NSMoS_2$ by functional coelomocytes of the earthworm *Eisenia fetida*. Considering that vacancy engineering is widely applied to enhance the $NSMoS_2$ performance, we assessed the potential role of such atomic vacancies in regulating cellular uptake processes. Coelomocyte internalization and lysosomal accumulation of $NSMoS_2$ were tracked by fluorescent labeling imaging. Cellular uptake inhibitors, proteomics, and transcriptomics helped to mechanistically distinguish vacancy-mediated endocytosis pathways. Specifically, Mo ions activated transmembrane transporter and ion-binding pathways, entering the coelomocyte through assisted diffusion. Unlike molybdate, pristine $NSMoS_2$ (P-$NSMoS_2$) induced protein polymerization and upregulated gene expression related to actin filament binding, which phenotypically initiated actin-mediated endocytosis. Conversely, vacancy-rich $NSMoS_2$ (V-$NSMoS_2$) were internalized by coelomocytes through a vesicle-mediated and energy-dependent pathway. Mechanistically, atomic vacancies inhibited mitochondrial transport gene expression and likely induced membrane stress, significantly enhancing endocytosis (20.3%, $p < 0.001$). Molecular dynamics modeling revealed structural and conformational damage of cytoskeletal protein caused by P-$NSMoS_2$, as well as the rapid response of transport protein to V-$NSMoS_2$. These findings demonstrate that earthworm functional coelomocytes can accumulate $NSMoS_2$ and directly mediate cytotoxicity and that atomic vacancies can alter the endocytic pathway and enhance cellular uptake by reprogramming protein response and gene expression patterns. This study provides an important mechanistic understanding of the ecological risks of $NSMoS_2$.

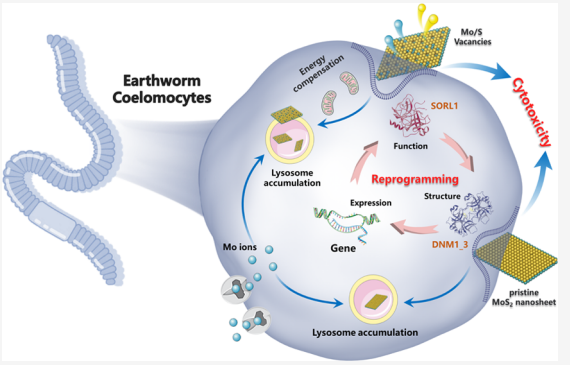

KEYWORDS: *earthworm coelomocytes, MoS_2 nanosheets, cellular uptake, atomic vacancies, proteins, molecular mechanisms*

INTRODUCTION

Engineered nanomaterials (ENMs) have many unique and highly useful properties that account for their versatile applications. However, the worldwide use of more than 200 million tons/year (projected to exceed 500 million tons/year by 2025) of these materials has raised significant concerns over the environmental and public health risks of ENMs.[1] Compared to conventional three-dimensional ENMs (e.g., the widely studied ZnO, CeO_2, TiO_2, etc.), two-dimensional molybdenum disulfide nanosheets ($NSMoS_2$) have attracted widespread interest in the fields of environmental protection, biomedicine, and material science due to their unique physicochemical, mechanical, and biological properties. This has increased their mass production and market deployment (global production exceeds 1.1×10^5 metric tons/year).[2−6] Considering the potentially large environmental and biological exposures and potential adverse impacts of $NSMoS_2$ throughout their life cycle, the environmental fate and effects, including biological mechanisms of action, must be prospectively evaluated.

The cellular behavior and intracellular localization of the nanoparticles are key determinants of their toxicity. Animal cells have been shown to absorb a wide range of ENMs. For example, SiO_2, Fe_2O_3, and polystyrene nanomaterials can enter human embryonic kidney cells, macrophages, and lung carcinoma epithelial cells through the scavenger receptor-mediated pathways.[7−10] However, two-dimensional nanoma-

Received: August 16, 2023
Revised: October 24, 2023
Accepted: November 13, 2023
Published: November 27, 2023

https://doi.org/10.1021/acs.est.3c06665
Environ. Sci. Technol. 2023, 57, 21637−21649

terials have a unique sheetlike morphology and are readily transformed. These materials may follow different cellular uptake pathways compared with traditional three-dimensional ENMs. $NSMoS_2$ (5−25 μg/mL) were reported to be absorbed by human (hepatoma HepG2) and algal (*Chlorella vulgaris*) cells.[11−14] However, the relationship between the cytotoxicity and the cellular internalization of $NSMoS_2$ is still uncertain. Membrane receptor proteins are known to play a key role in regulating endocytosis.[15,16] The protein response mechanisms, including expression pattern and structural response, for the cellular uptake of $NSMoS_2$ and how gene pathway activation regulates such mechanisms also remain largely unknown.

As with most ENMs, the soil will be the ultimate sink for $NSMoS_2$.[17] $NSMoS_2$ exert adverse effects on terrestrial plants, inhibiting the growth and nutrient uptake by maize (*Zea mays*) and reprogramming carbon and nitrogen metabolism in rice (*Oryza sativa* L.).[18,19] Soil invertebrates are generally recognized as more sensitive models for toxicity assessment than plants, allowing for a more dynamic exposure scenario. Earthworms are ubiquitous sentinel species in soil, providing an active defense against xenobiotics and coordinating the *in vivo* homeostasis mainly through the free-circulating coelomocytes in the coelom.[20,21] We have previously demonstrated that *Eisenia fetida* absorb $NSMoS_2$ via dermal and oral routes, with subsequent accumulation in the gut.[22] This whole-animal exposure to $NSMoS_2$ can alter the coelomocyte mitochondrial dynamics and inhibit the activity of complex III in the respiratory electron transport chain, further disrupting the cellular energy metabolic processes. Consequently, the functional coelomocytes represent a realistic exposure scenario and a sensitive target of toxic action. Further elucidating the cellular behavior and subcellular localization of $NSMoS_2$ in earthworm coelomocytes contributes to a better mechanistic understanding of their potential risks.

Vacancy design is an emerging engineering tool to tune and improve 2D ENM performance (e.g., catalysis, electrochemical activity, and pollutant adsorption, etc.) by providing additional physical and chemical reaction sites.[23−25] The design of vacancies includes single (e.g., sulfur vacancies) or aggregated atomic vacancies (e.g., surface defects and nanopores). $NSMoS_2$ are amenable for enhanced catalytic and photovoltaic properties through vacancy engineering due to their highly ordered lattice structure.[26,27] $NSMoS_2$ enriched with atomic vacancies may exhibit entirely distinct biological effects compared to pristine $NSMoS_2$.[11,22,28] For example, surface defects in $NSMoS_2$ induced stronger *in vivo* bioenergetic toxicity to earthworms, specifically increased rates of coelomocytes apoptosis.[22] Similarly, Shi et al. reported that nanopores on $NSMoS_2$ can enhance their antibacterial ability by facilitating electron transfer with biofilms.[29]

In the current study, we hypothesized that $NSMoS_2$ cellular uptake is responsible for cytotoxicity and that atomic vacancies can enhance the cellular internalization of $NSMoS_2$ by reprogramming the gene expression and the associated protein profile. Random atom vacancies were introduced on the lattice plane of $NSMoS_2$ by continuous ultraviolet (UV) irradiation. An established nanomorphology-specific fluorescent labeling approach coupled with high-resolution transmission electron microscopy was applied to provide visual and quantitative evidence of earthworm coelomocyte uptake and intracellular localization of $NSMoS_2$, as well as conventional Mo ions. Key proteins involved in cellular internalization were screened through high-throughput proteomics, and targeted interaction models were established by using molecular dynamics simulations. Finally, transcriptomics was used to characterize the molecular initiating events underlying the different cellular uptake mechanisms. This work contributes to a comprehensive elucidation of the cellular behavior and cytotoxicity mechanisms of $NSMoS_2$, which will enable an accurate understanding of associated risk and the efforts for the safe redesign of these important materials.

MATERIALS AND METHODS

Synthesis of Pristine and Vacancy-Rich $NSMoS_2$ and Fluorescent Labeling. P-$NSMoS_2$ were obtained from XFNANO Materials Tech. Co., Ltd., Jiangsu, China, and V-$NSMoS_2$ were prepared by UV irradiation (Text S1).[22] Two types of $NSMoS_2$ were characterized as detailed in Text S2. To visualize cellular uptake, fluorescence-labeled P-$NSMoS_2$ or V-$NSMoS_2$ were synthesized by a carboxylamine coupling reaction.[30] 1-(3-(Dimethylamino)propyl)-3-ethylcarbodiimide hydrochloride (2.5 mg/mL, Bidepharm, China), *N*-hydroxy succinimide (5 mg/mL, Nmrbio, China), and fluorescein isothiocyanate−bovine serum albumin (FITC-BSA, 2.5 mg/mL, Qiyue-Bio, China) were coreacted with P-$NSMoS_2$ or V-$NSMoS_2$ (2.5 mg/mL) and thoroughly dispersed. After magnetic stirring for 3 h at 25 °C in the dark, the labeled nanosheets were collected by centrifugation (20,000 rpm/10 min) and quantified to form a 5 mg Mo/mL stock solution using inductively coupled plasma−mass spectrometry (ICP-MS, iCAP-Q, Thermo Fisher).

Exposure Strategy. Adult earthworms (*E. fetida*; 5−8 months) were obtained from an earthworm breeding facility in Jurong, Jiangsu Province, China. After 14 days of domestication in artificial soil, coelomocytes were isolated using a noninvasive method as described in Text S3.[22] Coelomocytes (initial viability ≥95%, Figure S1) were coincubated with 50 μg Mo/mL as P-$NSMoS_2$, V-$NSMoS_2$, and their ionic counterpart (Na_2MoO_4) in a tailored culture medium (15% fetal bovine serum, 1% penicillin/streptomycin, 84% RPMI-1640) for 24 h at 20 ± 1 °C in dark conditions. This exposure concentration was verified by ICP-MS and was within the range of reported exposures (Table S1).

Transmission Electron Microscopy (TEM) Observation and Cellular Mo Quantification. After exposure, coelomocytes were sequentially treated with 2.5% glutaraldehyde and 1% osmium acid solutions to fix the original cellular morphology and ultrastructural characteristics. To avoid cell shrinkage and damage under vacuum conditions in TEM imaging, coelomocytes were dehydrated using gradients of anhydrous ethanol (50−70−90%). Subsequently, coelomocytes were embedded in resin/acetone mixtures (V/V = 1:1, 1:2, 1:3) to provide structural support for subsequent sectioning. After polymerization at 60 °C for 48 h, samples were sectioned on an ultrathin sectioning machine (EM-UC7, Leica, Germany) and stained before observation on a field emission transmission electron microscope (Talos-F200X-G2, Thermo Fisher). In addition, a sucrose density gradient centrifugation (SDGC) approach was used to effectively separate coelomocytes from surface-adsorbed and noningested nanosheets (detailed in Text S4).[12] The cell-associated Mo content measured by ICP-MS was normalized to μg/10^6 cells.

Laser Confocal Imaging. The fluorescence visualization tracking of P-$NSMoS_2$ and V-$NSMoS_2$ was performed with synthetic FITC-labeled nanomaterials under a multiphoton laser confocal microscope (TCS-SP8-STED-3X, Leica, Ger-

https://doi.org/10.1021/acs.est.3c06665
Environ. Sci. Technol. 2023, 57, 21637−21649

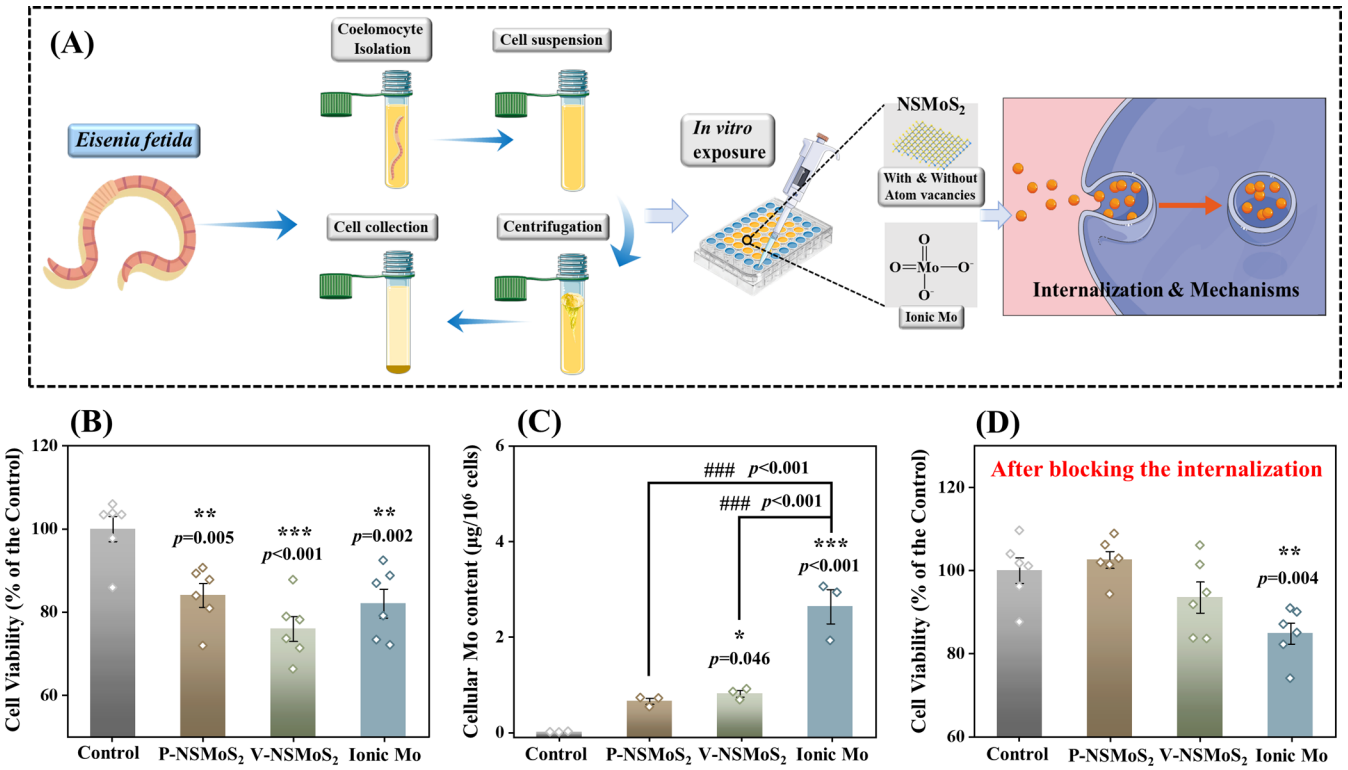

Figure 1. Earthworm (*E. fetida*) coelomocyte isolation procedures and exposure strategy (A). Cell viability (B) and corresponding total intracellular Mo content (C) per 10^6 cells upon exposure to pristine (P-$NSMoS_2$) and vacancy-rich (V-$NSMoS_2$) MoS_2 nanosheets, and ionic Mo at 50 μg Mo/mL for 24 h. Effect of copretreatment with physical and pharmacological inhibitors (see text for details) on the cytotoxicity of different Mo forms (D). Data are expressed as mean ± SEM ($n \geq 3$ biologically independent treatments). Significant differences between treatments and control are expressed as $^*p < 0.05$, $^{**}p < 0.01$, and $^{***/\#\#\#}p < 0.001$.

many). To further determine the subcellular localization of $NSMoS_2$, lysosomes were specifically illuminated by a LysoTracker (50 nM, Beyotime, China). Corresponding FITC fluorescence quantification data (normalized to 10^6 cells) were recorded by a microplate reader (SpectraMax-iD5, Thermo Fisher).

Identification of Internalization Pathways. Coelomocytes were pretreated with low temperature (4 °C), cytochalasin-D (CD; 5 μg/mL), chlorpromazine hydrochloride (CPZ; 10 μg/mL), methyl-β-cyclodextrin (MβCD; 20 mM), genistein (GST; 400 μM), and 5-(*N*-ethyl-*N*-isopropyl)-amiloride (EIPA; 10 μg/mL) for 2 h. The specific mechanisms of cellular uptake blockade by the above physical and pharmacological inhibitors are detailed in Text S5. Subsequently, FITC-labeled P-$NSMoS_2$ or V-$NSMoS_2$ and molybdate were added, and incubation continued for 24 h. After separating coelomocytes from nanosheets by the established SDGC approach, the cell-associated total Mo concentration and FITC intensity were quantified using ICP-MS and a microplate reader, respectively. The effects of the above physical and pharmacological inhibitors on cellular activity were assessed using the WST-8 probe (Solarbio, China) as detailed in Text S6.

High-Throughput Protein Screening and Molecular Mechanism Investigation. Cellular proteins were extracted using protein lysate (8 mol/L urea and 1% sodium dodecyl sulfate (SDS) with a protease inhibitor). Quality control of obtained proteins was achieved by SDS-polyacrylamide gel electrophoresis (SDS-PAGE) analysis and protein content measurement (Table S2). After alkylation and trypsin treatment, samples were analyzed by liquid chromatography coupled with tandem mass spectrometry (LC-MS/MS) using an EASY-nLC-1200 liquid phase system (Thermo Fisher) integrated with a timsTOF-Pro-2 mass spectrometer (Bruker, Germany). More specific proteomics testing procedures and instrument conditions are given in Text S7. For transcriptomic analysis, cellular RNA was extracted using TRIZOL reagent, and samples that met the quality requirements (total RNA ≥ 1 μg, RNA concentration ≥35 ng/μL, $OD_{260/280} \geq 1.8$, and $OD_{260/230} \geq 1.0$) were sequenced on the Illumina NovaSeq-6000 platform. Methods for RNA quality evaluation and sequencing are detailed in Text S8.

Molecular Modeling. Target proteins were screened based on the significance ranking among the largest enriched functional items as a function of treatment. Before molecular model establishment, the structures of P-$NSMoS_2$ and V-$NSMoS_2$ (Figure S2) were assembled in CCDC Mercury (V. 2022.2.0).[31] Water molecules and extraneous heteroatoms were removed from target proteins by UCSF Chimera software.[32] Simulated initial structures of protein@$NSMoS_2$ complexes were constructed and optimized using the PACKMOL modeling tool.[33] The molecular dynamics simulations were performed using the Gromacs (V. 5.1.5) open-source software package.[34] Additional specific simulation parameters are detailed in Text S9.

Statistical Analysis. One-way analysis of variance (ANOVA) or a *t* test in GraphPad Prism (V. 7.0) was used to determine the statistical significance of differences between treatments. For proteomic and transcriptomic data, high-confidence proteins or genes further screened by their

https://doi.org/10.1021/acs.est.3c06665
Environ. Sci. Technol. 2023, 57, 21637−21649

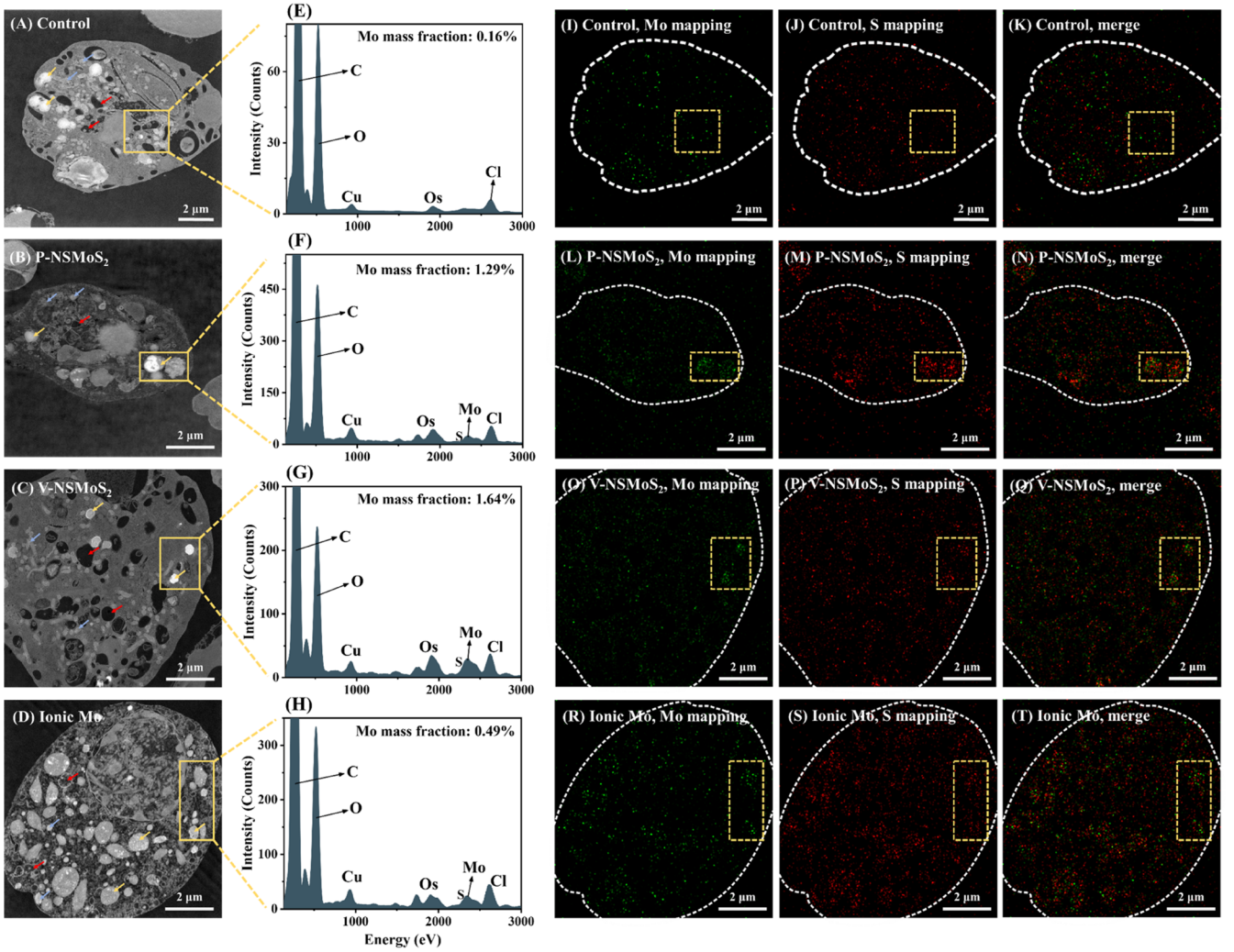

Figure 2. Transmission electron microscopy (TEM) evidence of the internalization of pristine (P-$NSMoS_2$) and vacancy-rich (V-$NSMoS_2$) MoS_2 nanosheets, and ionic Mo by earthworm (*E. fetida*) coelomocytes following exposure for 24 h at 50 μg Mo/mL. Representative TEM images of single coelomocytes (A–D). The yellow, blue, and red arrows represent lysosomes, mitochondria, and vesicles, respectively. Elemental spectrum (E–H) and mapping of Mo and S (I–T) of selected areas (yellow boxes).

expression in at least two biological replicates in at least one exposure group were used for subsequent analysis. Detailed bioinformatics analysis methods are given in Text S10.

RESULTS AND DISCUSSION

Characterization of P-$NSMoS_2$ and V-$NSMoS_2$. TEM images showed that P-$NSMoS_2$ had a flat surface with heterogeneous lateral dimensions (Figure S3A). UV irradiation caused random defect formation on the lattice basal plane of $NSMoS_2$ (Figure S3B), without significantly altering the average hydrodynamic diameter of the nanosheets (Figure S4). High-resolution TEM (HR-TEM, Figure S5) images accurately defined that these defects consisted of single or clustered Mo–S atom vacancies. Further characterizations showed that atomic vacancies also caused physical and microstructural property changes of $NSMoS_2$. The disorder and lattice spacing of V-$NSMoS_2$ were significantly greater (0.32 ± 0.017–0.46 ± 0.20 nm, $p < 0.05$) than those of P-$NSMoS_2$. A significant increase in the specific surface area (Figure S6, from 1.68 to 24.4 cm^2/g, $p < 0.05$) and surface roughness (Figure S7, from 140.9 to 564.6 pm, $p < 0.01$) of V-$NSMoS_2$ confirmed irregular edges associated with vacancies. The Raman peaks of P-$NSMoS_2$ at ~379 and ~405 cm^{-1} were blue-shifted by ~1.8 and ~3.8 cm^{-1} after UV irradiation, with the Raman A_{1g}/E^1_{2g} ratio increasing from 1.87 to 2.40 (Figure S8). These results indicate lattice distortion caused by vacancy creation.

Biological media may affect nanoparticle dissolution.[35] In the customized coelomocyte culture medium, the ionic-Mo release from P-$NSMoS_2$ at 50 μg Mo/mL (11.2 ± 0.37 μg Mo/mL) was significantly higher ($p < 0.001$) than from V-$NSMoS_2$ (4.30 ± 0.11 μg Mo/mL) over 24 h (Figure S9). This is in contrast to other reports in ultrapure water.[22,36] The nonsignificant change (n.s.) in hydrodynamic diameters (Figure S4) suggests that P-$NSMoS_2$ and V-$NSMoS_2$ dispersed equally well in the cell culture system within 24 h. Zeng et al. reported that the presence of nanocolloids significantly inhibited soluble Mo release from MoS_2 nanosheets in a BG-11 algal culture media.[12] Compared to P-$NSMoS_2$, V-$NSMoS_2$ possesses more abundant edge sites and a higher specific surface area. The abundant proteins in the coelomocyte culture medium may electrostatically stabilize the nanosheets by more tightly coating the V-$NSMoS_2$ surface and vacancy sites, thereby minimizing ion release and agglomeration.[37]

https://doi.org/10.1021/acs.est.3c06665
Environ. Sci. Technol. 2023, 57, 21637–21649

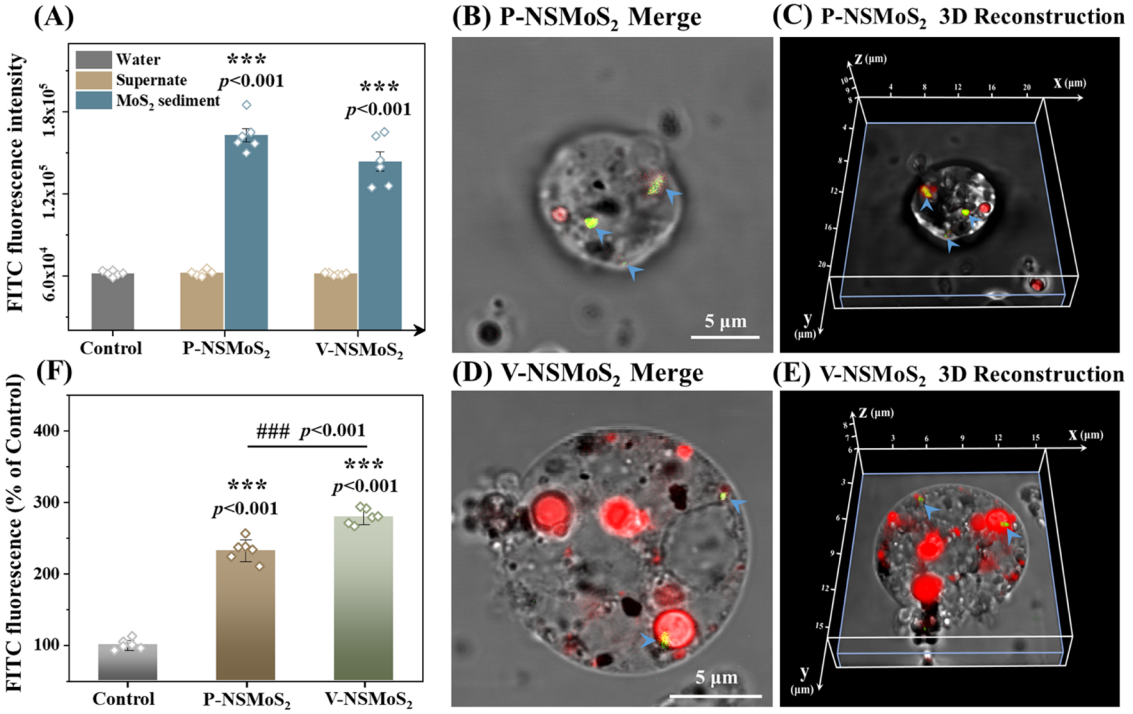

Figure 3. Quality assessment of fluorescein isothiocyanate (FITC)-labeled MoS_2 nanosheets ($NSMoS_2$) (A). Laser confocal captures (B, D) of FITC-labeled $NSMoS_2$ (green, highlighted by blue arrows) being internalized by earthworm (*E. fetida*) coelomocytes and colocalized with lysosomes (red). Three-dimensional reconstruction images of single cells (C, E) confirm that $NSMoS_2$ were located inside cells rather than overlapping fields of view. The total intracellular FITC fluorescence intensity (F) per 10^6 cells upon exposure to pristine (P-$NSMoS_2$) and vacancy-rich (V-$NSMoS_2$) MoS_2 nanosheets, and ionic Mo at 50 μg Mo/mL for 24 h. Data are expressed as mean ± SEM (n = 6). Significant differences between treatments and control are expressed as ***/### $p < 0.001$.

$NSMoS_2$ Cytotoxicity Requires Endocytosis. We developed a coelomocyte-based *in vitro* exposure protocol (Figure 1A) to investigate the relationship between $NSMoS_2$ cellular behavior and their toxicity. Coelomocyte viability significantly decreased to 84.0, 76.0, and 82.1% of the control following 24 h of *in vitro* exposure to 50 μg of Mo/mL P-$NSMoS_2$, V-$NSMoS_2$, and ionic Mo, respectively (Figure 1B). The cellular uptake of nanomaterials is thought to be an initiating event of cytotoxicity.[38,39] Our previous work reported the oxidative stress and energy metabolism disturbance in the coelomocytes as part of the overall response of earthworms upon *in vivo* exposure to $NSMoS_2$ and that vacancy defects enhanced such toxicity potential.[22] However, it is challenging to track the real-time interaction of $NSMoS_2$ with coelomocytes *in vivo*, thus hampering the effort to establish a mechanistic connection between the observed toxicity and cellular uptake behavior. In the present work, the uptake of different Mo forms by coelomocytes *in vitro* was quantified by ICP-MS (Figure 1C). The total intracellular Mo content was 0.01, 0.66 (n.s.), 0.81 ($p < 0.05$), and 2.64 ($p < 0.001$) $\mu g/10^6$ cells for the control, P-$NSMoS_2$, V-$NSMoS_2$, and molybdate groups, respectively. This suggests that the coelomocytes were susceptible to the uptake of different forms of Mo. Coelomocyte Mo content was significantly higher ($p < 0.001$) in the ionic control than in both $NSMoS_2$ groups, implying that the uptake of ions and nanosheets may follow different pathways.

Based on the above observations, we hypothesized that $NSMoS_2$-induced cytotoxicity can be attributed to the internalization of $NSMoS_2$. To test this hypothesis, potential active endocytosis and macropinocytosis pathways were blocked by pretreatment with a combination of physical (4 °C) and pharmacological inhibitors, including CD, CPZ, MβCD, GST, and EIPA.[12,30,40−42] After inhibitor addition, P-$NSMoS_2$ and V-$NSMoS_2$ no longer induced significant cell death, although the molybdate ion still exhibited cytotoxicity (Figure 1D, $p < 0.01$). This confirms that molybdate-induced loss of cell viability is independent of the endocytosis pathways involved with nanosheet accumulation. More specifically, unlike molybdate ions, P-$NSMoS_2$ and V-$NSMoS_2$ cytotoxicity requires endocytosis.

TEM Observation of Coelomocyte Uptake of P-$NSMoS_2$, V-$NSMoS_2$, and Na_2MoO_4. After the internalization process was identified to be responsible for $NSMoS_2$ cytotoxicity, the subcellular distribution of different Mo forms and the coelomocyte ultrastructure were investigated using TEM combined with energy-dispersive spectroscopy (EDS). The images of control earthworm coelomocytes (Figure 2A) show abundant and intact lysosomes, mitochondria, and intracellular vesicles. No significant cytoplasmic membrane and organelle damage was observed upon exposure to any of the Mo forms (Figure 2B−D). Several studies reported the uptake of MoS_2 and WS_2 nanosheets by *C. vulgaris* with TEM,[43,44] however, without definitive elemental identification. In the current study, we observed particles exhibiting a suspected $NSMoS_2$ morphology within the coelomocytes (Figure S10, red arrows), although subsequent EDS analysis did not identify Mo and S enrichment in these regions. We speculate that exogenous $NSMoS_2$ taken up by coelomocytes may rapidly interact with organelles or vesicles, subsequently undergoing biological processes such as encapsulation and digestion and ultimately losing their nanoscale morphology.

https://doi.org/10.1021/acs.est.3c06665
Environ. Sci. Technol. 2023, 57, 21637−21649

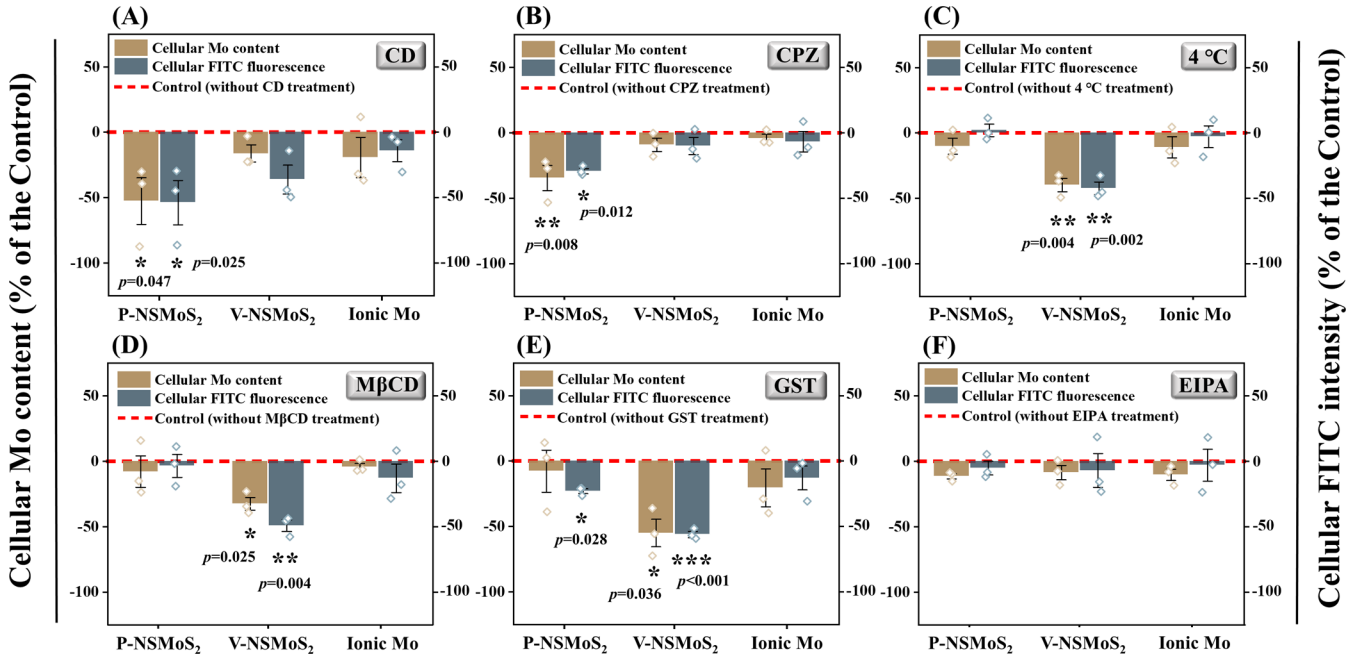

Figure 4. Differences in the internalization mechanisms of pristine (P-$NSMoS_2$) and vacancy-rich (V-$NSMoS_2$) MoS_2 nanosheets, and ionic Mo by earthworm (*E. fetida*) coelomocytes following exposure to different Mo forms at 50 μg Mo/mL for 24 h were distinguished by the quantification of intracellular Mo content and fluorescein isothiocyanate (FITC) intensity using different physical (low temperature) and pharmacological inhibitors, including CD: cytochalasin-D (A), CPZ: chlorpromazine hydrochloride (B), 4 °C treatment (C), MβCD: methyl-β-cyclodextrin (D), GST: genistein (E), and EIPA: 5-(*N*-ethyl-*N*-isopropyl)-amiloride (F). The data are expressed as mean ± SEM (n = 3 biologically independent treatments). Significant differences compared to the control group (without physical/pharmacological inhibitor pretreatment) are expressed as *p < 0.05, **p < 0.01, and ***p < 0.001.

The lysosomal region was first examined given the key role of these structures in phagocytosis and the digestion of xenobiotics.[45] The selected areas for the EDS spectra confirm Mo and S enrichment in lysosomes after P-$NSMoS_2$, V-$NSMoS_2$, and molybdate exposures as compared to the control (Figure 2E−H). In fact, cellular EDS mapping revealed that lysosomes were the primary accumulation sites (Figure 2I−T). The Mo signal was more evenly distributed within the cells in the molybdate group, whereas its lysosomal enrichment was clearly evident in the $NSMoS_2$ groups. This was further highlighted by the semiquantitative analysis of the lysosomal region elemental mass fraction, with the Mo mass fractions in P-$NSMoS_2$ and V-$NSMoS_2$ groups being 1.29 and 1.64%, respectively. This is higher than the Mo mass fraction of the molybdate (0.49%) and control (0.16%) groups.

Given the ionic release and potential intracellular digestion of $NSMoS_2$, a clear distinction between Mo ionic forms and nanoforms detected in the lysosomal region is necessary; TEM-EDS and ICP-MS provided insufficient evidence in this respect. To address this issue, we labeled P-$NSMoS_2$ and V-$NSMoS_2$ with FITC via a carboxylamine coupling reaction. This fluorescent labeling approach is tailored toward nanomorphology and facilitates efforts to track the cellular uptake and distribution of $NSMoS_2$.

Fluorescent Labeling Technique Demonstrates Coelomocyte Uptake of P-$NSMoS_2$ and V-$NSMoS_2$. Before exposure, we separated labeled $NSMoS_2$ from the associated suspension and evaluated the FITC labeling stability through fluorescence quantification. The supernatant fluorescence intensity was equivalent to that of the ultrapure water, whereas both types of labeled $NSMoS_2$ sediment emitted strong fluorescence (Figure 3A, p < 0.001). This result indicates that FITC was stably labeled on P-$NSMoS_2$ and V-$NSMoS_2$, without significant fluorescence leakage or release. Subsequent cell exposure experiments and laser confocal imaging exhibited the presence of two types of labeled nanosheets (green) in the bright-field coelomocyte region and colocalization with the illuminated lysosomes (red) (Figure 3B,D). Three-dimensional modeling was initiated by setting the z-axis within the field of view and scanning multiple layers consecutively; this analysis confirmed that the captured fluorescence signals from P-$NSMoS_2$ and V-$NSMoS_2$ were located inside the coelomocytes rather than the visual field overlap (Figure 3C,E). Fluorescent labeling of $NSMoS_2$ excludes the interference of released Mo ions, allowing bidirectional validation of the $NSMoS_2$ uptake results based on Mo and fluorescence quantification. Specifically, intracellular FITC fluorescence intensity quantification per 10^6 coelomocytes showed that the cellular uptake of V-$NSMoS_2$ was significantly greater (p < 0.001) than for P-$NSMoS_2$ (Figure 3F). This is consistent with a previous study reporting increased uptake of nanopore-rich $NSMoS_2$ relative to intact $NSMoS_2$ by *C. vulgaris*.[28] As noted above, UV irradiation induces abundant atomic defects on the $NSMoS_2$ basal plane, providing additional active sites and edge chemical bonds.[46] Considering the increased uptake of V-$NSMoS_2$ by earthworm coelomocytes, we suggest that atomic vacancy generation alters the cellular uptake pathway of $NSMoS_2$.

Uptake Pathways of Different Mo Forms. Physical and pharmacological inhibitors at nontoxic doses (Figure S11) were applied to investigate the uptake pathways in coelomocytes of different Mo forms. Total Mo content and FITC intensity were simultaneously measured for the orthogonal validation of the results. The addition of CD, an actin monomer polymerization inhibitor, decreased intra-

https://doi.org/10.1021/acs.est.3c06665
Environ. Sci. Technol. 2023, 57, 21637−21649

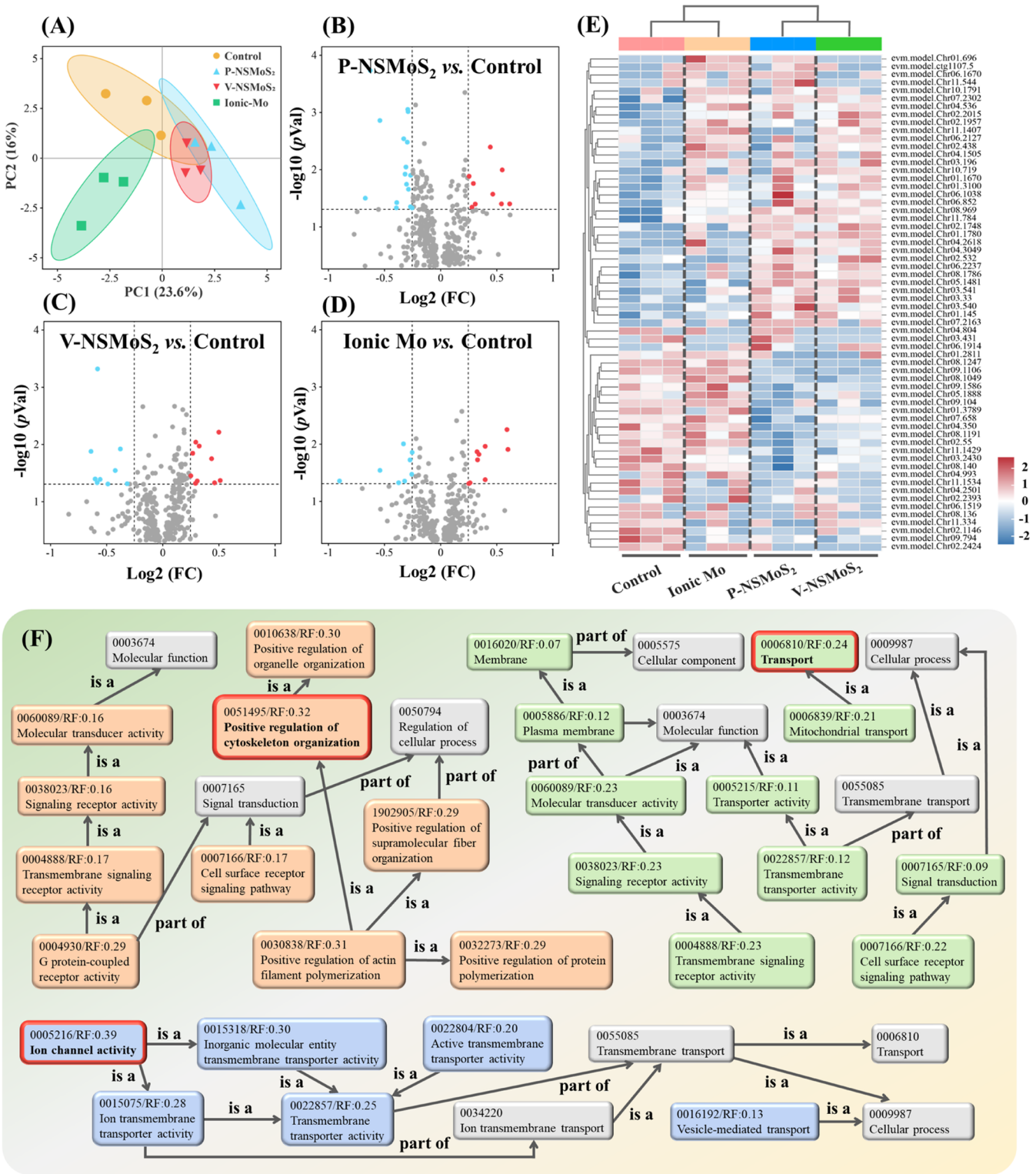

Figure 5. Proteomics analysis of earthworm (*E. fetida*) coelomocytes exposed to pristine (P-$NSMoS_2$) and vacancy-rich (V-$NSMoS_2$) MoS_2 nanosheets, and molybdate at 50 μg Mo/mL for 24 h. Principal components analysis (A) and volcano plots of all identified proteins form different comparisons (B–D). Blue and red dots indicate the significantly downregulated and upregulated proteins, respectively ($p < 0.05$ and $|Log2\ (FC)| > 0.25$); gray dots represent the protein with no significant changes. Hierarchical clustering analysis (E) of target proteins ($p < 0.05$). Proteins with $p < 0.05$ are matched according to their biological functions in the Gene Ontology (GO) database (F). Orange, green, and blue modules represent the enriched functions in P-$NSMoS_2$, V-$NSMoS_2$, and molybdate groups, respectively. The GO number and rich factors are included in each functional item, and the item with the largest rich factor is highlighted by the red border. For the relationships between different GO terms refer to http://geneontology.org/docs/ontology-relations/.

cellular Mo content and FITC intensity to −52.6% ($p < 0.05$) and −53.9% ($p < 0.05$) of the control (Figure 4A), respectively, confirming that the cellular uptake of P-$NSMoS_2$ involves actin-mediated endocytosis.[30,47] CPZ can

https://doi.org/10.1021/acs.est.3c06665
Environ. Sci. Technol. 2023, 57, 21637−21649

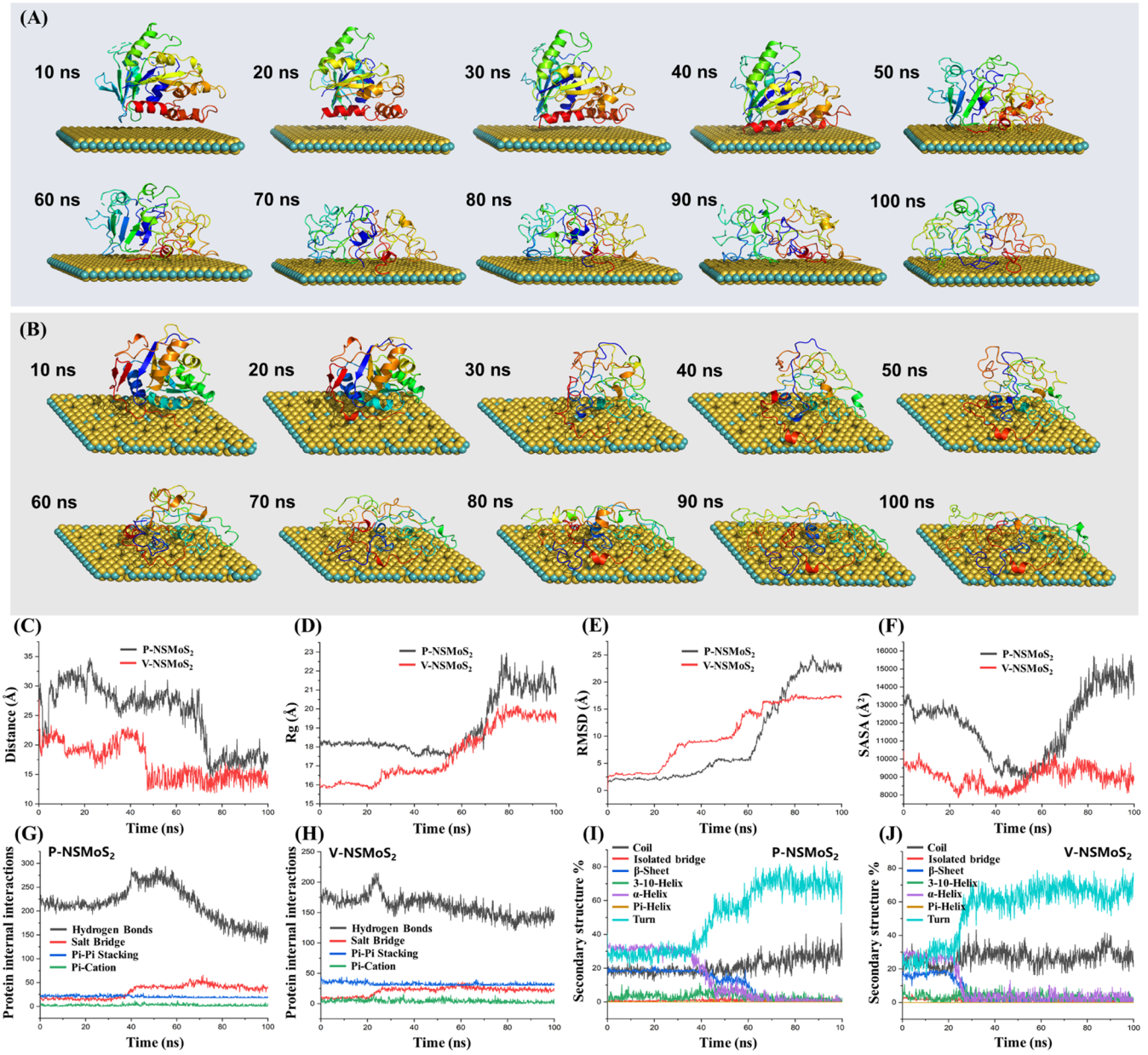

Figure 6. Molecular dynamics simulation results of pristine (P-NSMoS$_2$) and vacancy-rich (V-NSMoS$_2$) MoS$_2$ nanosheets with target proteins (DNM1_3 and SORL1). The target proteins were selected based on the functional items with the highest Gene Ontology (GO) rich factors from different comparisons (items marked with a red border in Figure 5F), and further ranking the protein *p*-values while satisfying the requirements of $p < 0.05$ and $|\text{Log2 (FC)}| > 0.25$. Representative snapshots for P-NSMoS$_2$@DNM1_3 and V-NSMoS$_2$@SORL1 binding systems during 100 ns of molecular dynamics simulation (A, B). P-NSMoS$_2$ possesses a complete substrate surface, with Mo and S atoms rendered in cyan and yellow. Mo and S atoms on V-NSMoS$_2$ were randomly exfoliated at a rate of ∼10% to form a defective basal plane. Time evolution of protein@nanosheets distance (C), protein radius of gyrate values (D), protein root-mean-square deviation values (E), and protein solvent-access surface area values (F). Changes in the protein internal interactions (G, H) and secondary structure (I, J) within the simulation interval.

impede clathrin-coated pit formation through a reversible translocation mechanism that relocates clathrin from the plasma membrane to intracellular vesicles.[40] After CPZ pretreatment, the cellular uptake of P-NSMoS$_2$ significantly decreased (Figure 4B, $p < 0.05$), suggesting a clathrin-mediated vesicular transport process. Unlike P-NSMoS$_2$, precooling at 4 °C caused a decrease of intracellular Mo content and FITC intensity in the V-NSMoS$_2$ group to −39.8% ($p < 0.01$) and −42.3% ($p < 0.01$) of the control, respectively (Figure 4C). This finding is indicative of an energy-dependent cellular uptake of V-NSMoS$_2$.[12] MβCD and GST can block caveolae-mediated endocytosis by disrupting the lipid raft integrity and inhibiting the recruitment of myosin II, respectively.[41,48,49] Pretreatment with MβCD and GST significantly reduced the coelomocyte uptake of V-NSMoS$_2$, implicating caveolae-mediated endocytosis ($p < 0.05$, Figure 4D,E). P-NSMoS$_2$ uptake was inconsistent with Mo content and FITC intensity evaluation following GST pretreatment (Figure 4E). In addition, blocking macropinocytosis with EIPA pretreatment did not significantly affect cellular uptake ability (Figure 4F), indicating that the uptake process of different Mo forms is independent of macropinocytosis.[42] Importantly, the cellular uptake of Mo ions does not involve any of the above pathways. Our data suggest that clathrin- and actin-mediated endocytosis

https://doi.org/10.1021/acs.est.3c06665
Environ. Sci. Technol. 2023, 57, 21637−21649

are responsible for the uptake of P-$NSMoS_2$ by coelomocytes, while caveolae-mediated endocytosis is the primary pathway for the energy-dependent uptake of V-$NSMoS_2$.

Protein Profile upon Exposure. High-throughput protein identification was conducted to further explore the underlying molecular mechanisms of differential coelomocyte uptake behavior. A principal component analysis (PCA) of all target proteins highlighted a significant separation between treatments and the control; in addition, P-$NSMoS_2$ and V-$NSMoS_2$ were slightly separated (Figure 5A), even without considering the effect of molybdate (Figure S12). Thresholds of $p < 0.05$ and $|\text{Log2 (FC)}| > 0.25$ were set, obtaining 59 (30 upregulated and 29 downregulated), 48 (24 upregulated and 24 downregulated), and 39 (21 upregulated and 18 downregulated) differentially expressed proteins (DEPs) in coelomocytes exposed to P-$NSMoS_2$, V-$NSMoS_2$, and molybdate, respectively (Tables S3−S5 and Figure 5B−D). Hierarchical clustering (HCL) analysis (Figure 5E) and Venn maps (Figure S13) based on proteins of $p < 0.05$ further demonstrated that the cellular protein response to $NSMoS_2$ exposure was significantly different from that of molybdate and the controls.

The proteins with $p < 0.05$ from different treatments were matched in the Gene Ontology (GO) database to isolate the specific impacted biological functions. The overlapping biological functions affected by P-$NSMoS_2$ and V-$NSMoS_2$ involve the activity of transmembrane or cell surface signaling receptors and molecular sensors (Figure 5F). These functions constitute the initiating events of cellular endocytosis.[50] Separate from the shared functional impacts, P-$NSMoS_2$ specifically affected G-protein-coupled receptors (GPCRs) and protein polymerization, particularly actin. GPCRs have been reported to be involved in various cellular signaling processes and play a key role in maintaining cellular homeostasis.[51] Actin polymerization is one of the key pathways in cellular endocytosis.[52,53] Upregulation of cellular actin polymerization upon P-$NSMoS_2$ exposure promotes endocytic action, which is validated by results from actin inhibitor CD addition, as discussed above. Positive regulation of the cellular cytoskeleton was also enriched in the P-$NSMoS_2$ group, indicating that cellular uptake processes caused potential stress to the cellular morphology. Unlike P-$NSMoS_2$, V-$NSMoS_2$ specifically induced membrane stress and mitochondrial motility processes. Sun et al. demonstrated that surface defects induced by UV irradiation can enhance the *in vivo* bioenergetic toxicity of $NSMoS_2$ for earthworm coelomocytes, including stronger electron-transfer interference and ROS accumulation.[22] The impacted biological pathway was verified by assaying cellular uptake at low temperatures (Figure 4C), demonstrating that the V-$NSMoS_2$ uptake is associated with energy consumption. Target proteins in the molybdate group were significantly enriched in ion channels and transmembrane transport functions. Ions enter cells primarily through two mechanisms: active transport (ATP-dependent) and facilitated diffusion (requiring ion channels, but not ATP).[54] Given the absence of observed energy dependence (Figure 4C), Mo ion uptake is an assisted diffusion process. Importantly, there were no shared enrichment functions between $NSMoS_2$ and molybdate, highlighting nanospecific effects that distinguish $NSMoS_2$ from conventional Mo ions.

Identification of Key Functional Proteins and Molecular Interaction Model Construction. Protein structural changes are an important factor affecting overall function.[55] Given this, we attempted to further mechanistically characterize the interaction processes of different Mo forms with key proteins involved in cellular uptake. Through high-throughput proteomics, we identified DNM1_3, SORL1, and VPS4 as key functional proteins impacted by exposure to P-$NSMoS_2$, V-$NSMoS_2$, and molybdate, respectively (abundances are shown in Figure S14, sequence match >80%) responsible for cytoskeleton organization, transport, and ion binding, respectively. Snapshots of molecular dynamics simulations of DNM1_3@P-$NSMoS_2$ and SORL1@V-$NSMoS_2$ every 10 ns showed that the distance between proteins and the nanosheet substrate gradually decreased and stabilized within ∼80 ns (Figure 6A,B). Distance quantification of the proteins and two $NSMoS_2$ centers of mass (Figure 6C) confirms the adsorption process. The protein radius of gyrate (R_g) during 100 ns reveals that two types of $NSMoS_2$ induced protein structural loosening (ΔR_g = 2.95−3.35 Å) upon interaction (Figure 6D). The root-mean-square deviation (RMSD, Figure 6E) fluctuations support the above observations and further determine that the deformation of DNM1_3 (ΔRMSD = 23.2 Å) with P-$NSMoS_2$ was greater than that of SORL1 adsorbed on V-$NSMoS_2$ (ΔRMSD = 17.2 Å). P-$NSMoS_2$ caused a decrease in the solvent-access surface area (SASA, Figure 6F) of DNM1_3 from 0 to 50 ns, followed by an increase that exceeded the initial SASA value (13016−14248 $Å^2$). Compared to P-$NSMoS_2$, V-$NSMoS_2$ caused a decrease in the SORL1 SASA value (10447−8907 $Å^2$) at 100 ns. This signifies an expansion of the macromolecular exposed region in the P-$NSMoS_2$@DNM1_3 system, while the proteins were encapsulated more tightly with a hydrophobic surface in the V-$NSMoS_2$@SORL1 system. Unlike the V-$NSMoS_2$@SORL1 system, the dramatic binding energy fluctuation during the stable phase (80−100 ns) of the P-$NSMoS_2$@DNM1_3 system suggests an instability of binding, which may affect the interaction patterns of amino acids within the protein (Figure S15).

We further counted the number of hydrogen bonds formed, salt bridges, $\pi-\pi$ stacking, and π-cation interactions in the two binding systems (Figure 6G,H). Hydrogen bonding is the main form of the amino acid interaction inside the two proteins. P-$NSMoS_2$ caused changes in the hydrogen bonds and salt bridge amounts of DNM1_3 at ∼40−60 ns, which is later than that of the V-$NSMoS_2$@SORL1 system (∼20−30 ns). The stability of amino acid interactions within proteins is essential for maintaining a functional secondary structure.[56] The secondary structure of DNM1_3 was significantly changed at ∼40 ns, while the change onset of SORL1 was at ∼20 ns (Figure 6I,J). Consistent with the snapshots in Figure 6A,B, the secondary structures of DNM1_3 and SORL1 changed with similar patterns, showing a content increase in the turning angle (31.7−50.5%), along with a decrease of the α-helix (25.3−26.0%), and complete disappearance of the β-sheet (Figure S16).

Considering the ion release of P-$NSMoS_2$ and V-$NSMoS_2$, the dominant binding sites of MoO_4^{2-} on DNM1_3, SORL1, and VPS4, and the detailed binding microenvironment were further analyzed (Figure S17). The results showed that MoO_4^{2-} was preferentially bound to the surfaces of DNM1_3, SORL1, and VPS4 and that the binding was mainly driven by hydrogen bonding. Lysine, histidine, and serine were the key amino acids in DNM1_3, while arginine in SORL1 and VPS4 was responsible for ion binding. Overall, the conformational damage of cytoskeletal protein DNM1_3 upon P-$NSMoS_2$ binding (including secondary junction destruction and increased structural loosening/deformation/exposure)

https://doi.org/10.1021/acs.est.3c06665
Environ. Sci. Technol. 2023, 57, 21637−21649

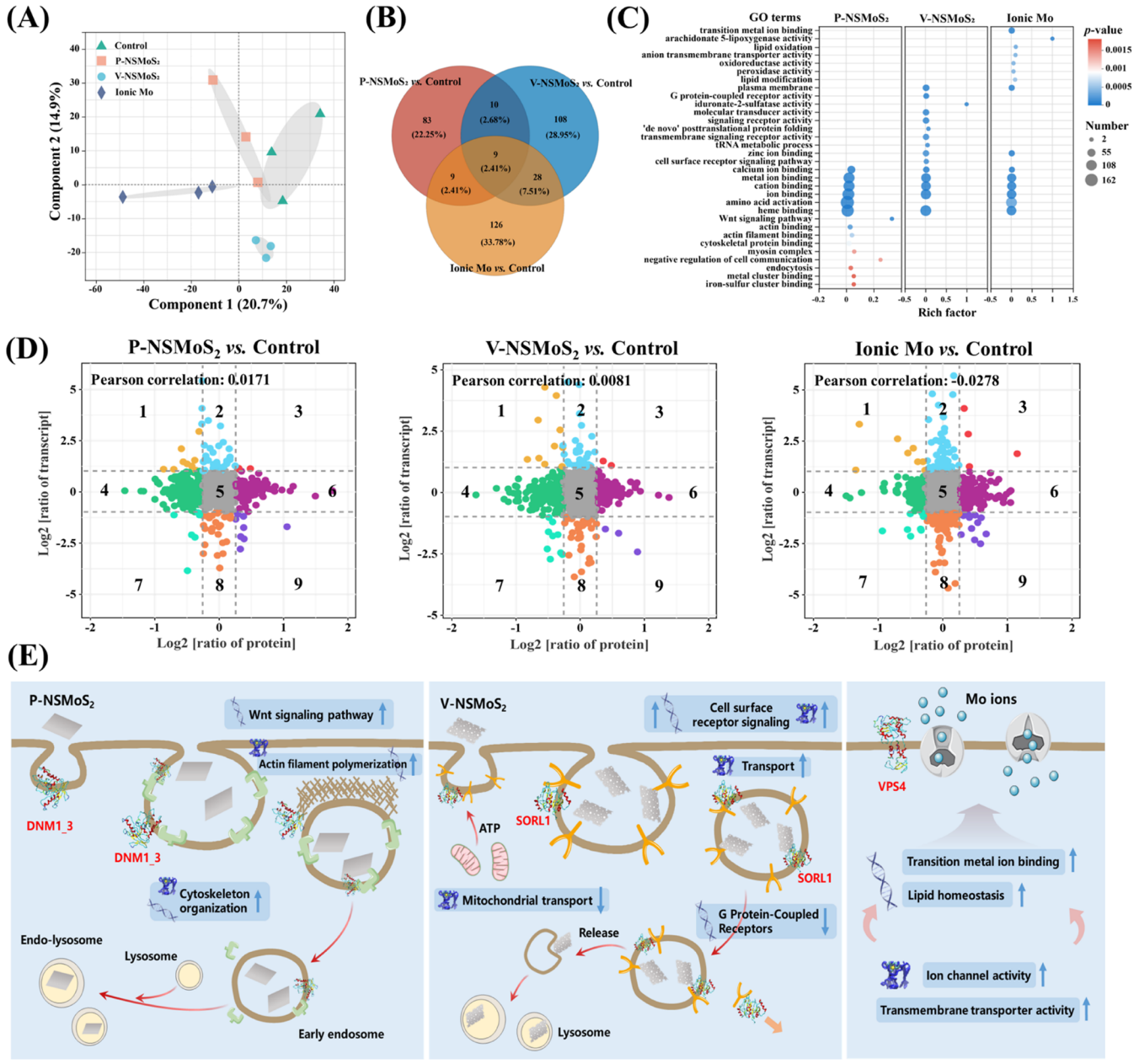

Figure 7. Transcriptomics results of earthworm (*E. fetida*) coelomocytes exposed to pristine (P-$NSMoS_2$) and vacancy-rich (V-$NSMoS_2$) MoS_2 nanosheets, and Na_2MoO_4, involving partial least-squares discrimination analysis (A), Venn plot (B), and Gene Ontology (GO) enrichment analysis (C). Nine-quadrant maps based on combined transcriptomics and proteomics analysis from different comparisons (D). The numbers in the plots define the different quadrants. Schematic presentation of the mechanistic differences of coelomocyte uptake of P-$NSMoS_2$, V-$NSMoS_2$, and Mo ions (E).

may lead to cellular morphological stress.[57] The earlier onset of structural changes in SORL1 upon cellular uptake of V-$NSMoS_2$ implies a rapid response of the transport protein to exposure, whereas the potential binding of soluble MoO_4^{2-} mediates the processes described above.

Coupled Transcriptomics and Proteomics Described the Molecular Initiation Events of Cellular Uptake. Transcriptomics was applied to further identify the molecular initiation events behind the differential protein response. Partial least-squares discrimination analysis (PLS-DA) of all identified 8676 unigenes demonstrated a clear separation of the three Mo form treatments (Figure 7A). A total of 111, 155, and 172 differentially expressed genes (DEGs, $p < 0.05$ and $|\text{Log2 (FC)}| > 1$) were obtained in control vs P-$NSMoS_2$, control vs V-$NSMoS_2$, and control vs Na_2MoO_4 comparisons (Tables S6−S8). Volcano maps highlighted that $NSMoS_2$ (upregulation/downregulation ratio = 0.56) caused more gene downregulation than molybdate exposure (upregulation/downregulation ratio = 0.93) and that atomic vacancy creation increased this regulate pattern (upregulation/downregulation ratio = 0.52) (Figure S18). Importantly, the DEGs shared among P-$NSMoS_2$, V-$NSMoS_2$, and molybdate groups (2.41−7.51%) were significantly fewer than those possessed individually (22.25−33.78%) (Figure 7B). These results confirm the significant differences in coelomocyte gene expression patterns as a function of the Mo form.

The GO functional enrichment analysis revealed that DEGs in the P-$NSMoS_2$, V-$NSMoS_2$, and molybdate groups were

https://doi.org/10.1021/acs.est.3c06665
Environ. Sci. Technol. 2023, 57, 21637−21649

collectively enriched in the metal (cation) ion-binding pathways (Figure 7C). The DEGs in the molybdate group were related to the ion (metal) transmembrane transport pathway and specifically reshaped the lipid homeostasis of the cell membrane. Previous lipidomics-based analyses have reported similar results that ionic-Mo species can induce earthworm coelomocyte membrane stress by inhibiting membrane-related glycerophospholipid synthesis and down-regulating the fatty acid synthesis pathway.[58] Compared to conventional molybdate, DEGs in the P-$NSMoS_2$ group were associated with cytoskeletal protein and actin filament binding processes, which phenotypically induced potential cytoskeletal stress and actin-mediated endocytosis (Figures 4A and 5F). Additionally, the Wnt pathway was activated by P-$NSMoS_2$ exposure. The Wnt pathway is closely related to surface receptor-mediated intracellular and extracellular signaling,[59] in line with the impact of P-$NSMoS_2$ on coelomocyte surface receptor proteins and transmembrane signaling pathways (Figure 5F). Unlike P-$NSMoS_2$, the specific functional enrichment in the V-$NSMoS_2$ group involved membrane receptor signaling. In spite of the absence of phenotypic protein expression, the inhibited GPCR pathway predicted potential coelomocyte homeostasis stress upon V-$NSMoS_2$ exposure.

Transcriptomics and proteomics data were then integrated to reveal the joint regulation of the transcription−translation processes. More genes and proteins with opposite regulatory trends were seen in the P-$NSMoS_2$ group than in the V-$NSMoS_2$ group (1/9 quadrants, Figure 7D), suggesting that vacancies may reduce posttranscriptional regulation and translational modification processes. Considering that similar patterns were observed in the molybdate group (Figure 7D), as well as greater ion release from P-$NSMoS_2$ (Figure S9), the additional impacts of soluble Mo species on transcription and translation deserve attention.

Environmental Implications. As an emerging advanced functional nanomaterial, the widespread use of $NSMoS_2$ should be fully evaluated against ecological and public-health-associated risks. Soil biota are likely to be potential targets for $NSMoS_2$ exposure. Therefore, fully elucidating the mechanisms of $NSMoS_2$ toxicity to soil organisms will contribute to a comprehensive understanding of their risk profile. Cellular uptake and intracellular accumulation are initiating events and key mechanisms for nanoparticle toxicity.[60,61] Here, we demonstrate that 50 μg Mo/mL of $NSMoS_2$ exhibits significant cytotoxicity ($p < 0.01$) on *E. fetida* functional coelomocytes. Using a range of cellular endocytosis inhibitors, we further determined that $NSMoS_2$ cytotoxicity is dependent on endocytosis. A fluorescent labeling method that is specific to the nanomorphology was integrated with high-resolution TEM to provide conclusive visual evidence of $NSMoS_2$ uptake and lysosomal accumulation. Single or aggregated atom vacancies on the lattice basal plane significantly enhanced $NSMoS_2$ performance.[25,29] Thus, the role of these atomic vacancies in the toxicity profile of $NSMoS_2$ must be understood. Through the use of cellular endocytosis inhibitors and the integration of proteomics, molecular dynamics modeling, and transcriptomics, we successfully characterized the different mechanisms of cellular uptake of P-$NSMoS_2$, V-$NSMoS_2$, and conventional Mo ions (Figure 7E). Mo ion exposure activated ion channel and transmembrane transporter pathways at the protein and transcriptional levels, thereby entering coelomocytes through assisted diffusion. Compared to conventional molybdate, P-$NSMoS_2$ enhanced the protein polymerization process. Genes associated with actin filament binding and cytoskeletal protein reorganization were activated, which were manifested phenotypically as actin- and clathrin-mediated endocytic pathways. Unlike P-$NSMoS_2$, coelomocyte uptake of V-$NSMoS_2$ was associated with vesicle-mediated endocytosis and was energy-dependent. Quantitative results showed that the cellular internalization of V-$NSMoS_2$ was 20.3% greater than that of P-$NSMoS_2$ ($p < 0.001$). Mechanistically, V-$NSMoS_2$ specifically upregulated cell surface receptor signaling but repressed mitochondrial-transport-related genes, resulting in potential energy deprivation. Molecular dynamics modeling revealed structural and conformational damage to key cytoskeletal proteins upon P-$NSMoS_2$ exposure and a rapid response to V-$NSMoS_2$ of transport proteins with endocytosis. There is strong visual and quantitative evidence of $NSMoS_2$ uptake by earthworm functional coelomocytes, demonstrating a direct relationship between internalization and cytotoxicity. We found that induced atom vacancies altered the coelomocyte endocytosis pathway and enhanced $NSMoS_2$ uptake by reprogramming the protein responses and molecular initiation events. Given the close relationship between cytotoxicity and cellular internalization, further development of *in situ* imaging techniques is needed to validate the crucial role of *in vivo* cellular behavior regulation in $NSMoS_2$ toxicity.

■ ASSOCIATED CONTENT

Supporting Information

The Supporting Information is available free of charge at https://pubs.acs.org/doi/10.1021/acs.est.3c06665.

Supporting methods, coelomocyte live/dead imaging, modeling crystal structures, TEM/HR-TEM images, hydrodynamic diameters, specific surface area, surface roughness, Raman spectra, and ionic-Mo dissolution of P-$NSMoS_2$ and V-$NSMoS_2$; suspected snapshots of $NSMoS_2$ in coelomocytes; viability of coelomocytes exposed to physical and pharmacological inhibitors; PCA analysis, Venn maps, and key protein abundance for proteomics; binding energy and protein secondary structure changes in molecular dynamics simulation; molecular docking results; volcano plots of transcriptomics; literature basis for exposure concentration selection; quality control of proteomics; and significantly changed proteins and genes (PDF)

■ AUTHOR INFORMATION

Corresponding Author

Hao Qiu − *School of Environmental Science and Engineering, Shanghai Jiao Tong University, Shanghai 200240, China;* orcid.org/0000-0002-4743-9702; Email: haoqiu@sjtu.edu.cn

Authors

Kailun Sun − *School of Environmental Science and Engineering, Shanghai Jiao Tong University, Shanghai 200240, China*

Jason C. White − *The Connecticut Agricultural Experiment Station, New Haven, Connecticut 06504, United States;* orcid.org/0000-0001-5001-8143

https://doi.org/10.1021/acs.est.3c06665
Environ. Sci. Technol. 2023, 57, 21637−21649

Erkai He − *School of Geographic Sciences, East China Normal University, Shanghai 200241, China;* orcid.org/0000-0002-4866-3001

Cornelis A. M. Van Gestel − *Faculty of Science, Amsterdam Institute for Life and Environment (A-LIFE), Vrije Universiteit, Amsterdam 1081 HV, The Netherlands;* orcid.org/0000-0002-5651-0208

Peng Zhang − *School of Geography, Earth and Environmental Sciences, University of Birmingham, Edgbaston, Birmingham B15 2TT, United Kingdom; Department of Environmental Science and Engineering, University of Science and Technology of China, Hefei 230026, China;* orcid.org/0000-0002-2774-5534

Willie J.G.M. Peijnenburg − *National Institute of Public Health and the Environment, Center for the Safety of Substances and Products, Bilthoven 3720 BA, The Netherlands; Institute of Environmental Sciences, Leiden University, Leiden 2300 RA, The Netherlands;* orcid.org/0000-0003-2958-9149

Complete contact information is available at: https://pubs.acs.org/10.1021/acs.est.3c06665

Notes

The authors declare no competing financial interest.

■ ACKNOWLEDGMENTS

This study was financially supported by the National Natural Science Foundation of China (nos. 42022057, 42277117). H.Q. would like to thank for the sponsorship by the Oceanic Interdisciplinary Program of Shanghai Jiao Tong University.

■ REFERENCES

(1) Janković, N. Z.; Plata, D. L. Engineered Nanomaterials in the Context of Global Element Cycles. *Environ. Sci.: Nano* **2019**, *6* (9), 2697−2711.

(2) Huang, C.-C.; Al-Saab, F.; Wang, Y.; Ou, J.-Y.; Walker, J. C.; Wang, S.; Gholipour, B.; Simpson, R. E.; Hewak, D. W. Scalable High-Mobility MoS_2 Thin Films Fabricated by an Atmospheric Pressure Chemical Vapor Deposition Process at Ambient Temperature. *Nanoscale* **2014**, *6* (21), 12792−12797.

(3) Cao, M.; Cai, R.; Zhao, L.; Guo, M.; Wang, L.; Wang, Y.; Zhang, L.; Wang, X.; Yao, H.; Xie, C.; Cong, Y.; Guan, Y.; Tao, X.; Wang, Y.; Xu, S.; Liu, Y.; Zhao, Y.; Chen, C. Molybdenum Derived from Nanomaterials Incorporates into Molybdenum Enzymes and Affects Their Activities *in Vivo*. *Nat. Nanotechnol.* **2021**, *16* (6), 708−716.

(4) Xu, Z.; Lu, J.; Zheng, X.; Chen, B.; Luo, Y.; Tahir, M. N.; Huang, B.; Xia, X.; Pan, X. A Critical Review on the Applications and Potential Risks of Emerging MoS_2 Nanomaterials. *J. Hazard. Mater.* **2020**, *399*, No. 123057.

(5) Radisavljevic, B.; Radenovic, A.; Brivio, J.; Giacometti, V.; Kis, A. Single-Layer MoS_2 Transistors. *Nat. Nanotechnol.* **2011**, *6* (3), 147−150.

(6) Wang, Z.; Mi, B. Environmental Applications of 2D Molybdenum Disulfide (MoS_2) Nanosheets. *Environ. Sci. Technol.* **2017**, *51* (15), 8229−8244.

(7) Oh, N.; Park, J.-H. Endocytosis and Exocytosis of Nanoparticles in Mammalian Cells. *Int. J. Nanomed.* **2014**, *9*, 51−63.

(8) Lara, S.; Perez-Potti, A.; Herda, L. M.; Adumeau, L.; Dawson, K. A.; Yan, Y. Differential Recognition of Nanoparticle Protein Corona and Modified Low-Density Lipoprotein by Macrophage Receptor with Collagenous Structure. *ACS Nano* **2018**, *12* (5), 4930−4937.

(9) Prapainop, K.; Miao, R.; Åberg, C.; Salvati, A.; Dawson, K. A. Reciprocal Upregulation of Scavenger Receptors Complicates Interpretation of Nanoparticle Uptake in Non-Phagocytic Cells. *Nanoscale* **2017**, *9* (31), 11261−11268.

(10) Lunov, O.; Zablotskii, V.; Syrovets, T.; Röcker, C.; Tron, K.; Nienhaus, G. U.; Simmet, T. Modeling Receptor-Mediated Endocytosis of Polymer-Functionalized Iron Oxide Nanoparticles by Human Macrophages. *Biomaterials* **2011**, *32* (2), 547−555.

(11) Zou, W.; Wan, Z.; Yu, X.; Liu, Z.; Yuan, P.; Zhang, X. Sulfur Vacancies Affect the Environmental Fate, Corona Formation, and Microalgae Toxicity of Molybdenum Disulfide Nanoflakes. *J. Hazard. Mater.* **2021**, *419*, No. 126499.

(12) Zeng, H.; Hu, X.; Ouyang, S.; Zhou, Q. Nanocolloids, but Not Humic Acids, Augment the Phytotoxicity of Single-Layer Molybdenum Disulfide Nanosheets. *Environ. Sci. Technol.* **2021**, *55* (2), 1122−1133.

(13) Zou, W.; Li, X.; Li, C.; Sun, Y.; Zhang, X.; Jin, C.; Jiang, K.; Zhou, Q.; Hu, X. Influence of Size and Phase on the Biodegradation, Excretion, and Phytotoxicity Persistence of Single-Layer Molybdenum Disulfide. *Environ. Sci. Technol.* **2020**, *54* (19), 12295−12306.

(14) Liu, S.; Shen, Z.; Wu, B.; Yu, Y.; Hou, H.; Zhang, X.-X.; Ren, H. Cytotoxicity and Efflux Pump Inhibition Induced by Molybdenum Disulfide and Boron Nitride Nanomaterials with Sheetlike Structure. *Environ. Sci. Technol.* **2017**, *51* (18), 10834−10842.

(15) Rennick, J. J.; Johnston, A. P. R.; Parton, R. G. Key Principles and Methods for Studying the Endocytosis of Biological and Nanoparticle Therapeutics. *Nat. Nanotechnol.* **2021**, *16* (3), 266−276.

(16) Alnasser, F.; Castagnola, V.; Boselli, L.; Esquivel-Gaon, M.; Efeoglu, E.; McIntyre, J.; Byrne, H. J.; Dawson, K. A. Graphene Nanoflake Uptake Mediated by Scavenger Receptors. *Nano Lett.* **2019**, *19* (2), 1260−1268.

(17) Gottschalk, F.; Sonderer, T.; Scholz, R. W.; Nowack, B. Modeled Environmental Concentrations of Engineered Nanomaterials (TiO_2, ZnO, Ag, CNT, Fullerenes) for Different Regions. *Environ. Sci. Technol.* **2009**, *43* (24), 9216−9222.

(18) Chen, S.; Kang, Z.; Peralta-Videa, J. R.; Zhao, L. Environmental Implication of MoS_2 Nanosheets: Effects on Maize Plant Growth and Soil Microorganisms. *Sci. Total Environ.* **2023**, *860*, No. 160362.

(19) Zhao, L.; Chen, S.; Tan, X.; Yan, X.; Zhang, W.; Huang, Y.; Ji, R.; White, J. C. Environmental Implications of MoS_2 Nanosheets on Rice and Associated Soil Microbial Communities. *Chemosphere* **2022**, *291*, No. 133004.

(20) Hayashi, Y.; Engelmann, P.; Foldbjerg, R.; Szabó, M.; Somogyi, I.; Pollák, E.; Molnár, L.; Autrup, H.; Sutherland, D. S.; Scott-Fordsmand, J.; Heckmann, L.-H. Earthworms and Humans *in Vitro*: Characterizing Evolutionarily Conserved Stress and Immune Responses to Silver Nanoparticles. *Environ. Sci. Technol.* **2012**, *46* (7), 4166−4173.

(21) Stürzenbaum, S. R.; Georgiev, O.; Morgan, A. J.; Kille, P. Cadmium Detoxification in Earthworms: From Genes to Cells. *Environ. Sci. Technol.* **2004**, *38* (23), 6283−6289.

(22) Sun, K.; White, J. C.; He, E.; Van Gestel, C. A. M.; Qiu, H. Surface Defects Regulate the *in Vivo* Bioenergetic Response of Earthworm *Eisenia fetida* Coelomocytes to Molybdenum Disulfide Nanosheets. *ACS Nano* **2023**, *17* (3), 2639−2652.

(23) Zhu, Q.; Chen, W.; Cheng, H.; Lu, Z.; Pan, H. WS_2 Nanosheets with Highly-Enhanced Electrochemical Activity by Facile Control of Sulfur Vacancies. *ChemCatChem* **2019**, *11* (11), 2667−2675.

(24) Fei, H.; Guo, T.; Xin, Y.; Wang, L.; Liu, R.; Wang, D.; Liu, F.; Wu, Z. Sulfur Vacancy Engineering of MoS_2 via Phosphorus Incorporation for Improved Electrocatalytic N_2 Reduction to NH_3. *Appl. Catal., B* **2022**, *300*, No. 120733.

(25) Hu, J.; Yu, L.; Deng, J.; Wang, Y.; Cheng, K.; Ma, C.; Zhang, Q.; Wen, W.; Yu, S.; Pan, Y.; Yang, J.; Ma, H.; Qi, F.; Wang, Y.; Zheng, Y.; Chen, M.; Huang, R.; Zhang, S.; Zhao, Z.; Mao, J.; Meng, X.; Ji, Q.; Hou, G.; Han, X.; Bao, X.; Wang, Y.; Deng, D. Sulfur Vacancy-Rich MoS_2 as a Catalyst for the Hydrogenation of CO_2 to Methanol. *Nat. Catal.* **2021**, *4* (3), 242−250.

(26) Cao, F.; Zhang, L.; Wang, H.; You, Y.; Wang, Y.; Gao, N.; Ren, J.; Qu, X. Defect-Rich Adhesive Nanozymes as Efficient Antibiotics for Enhanced Bacterial Inhibition. *Angew. Chem., Int. Ed.* **2019**, *58* (45), 16236−16242.

(27) Son, T.; Lee, D.; Lee, C.; Moon, G.; Ha, G. E.; Lee, H.; Kwak, H.; Cheong, E.; Kim, D. Superlocalized Three-Dimensional Live Imaging of Mitochondrial Dynamics in Neurons Using Plasmonic Nanohole Arrays. *ACS Nano* **2019**, *13* (3), 3063−3074.
(28) Tong, Y.; Feng, A.; Hou, X.; Zhou, Q.; Hu, X. Nanoholes Regulate the Phytotoxicity of Single-Layer Molybdenum Disulfide. *Environ. Sci. Technol.* **2019**, *53* (23), 13938−13948.
(29) Shi, T.; Hou, X.; Guo, S.; Zhang, L.; Wei, C.; Peng, T.; Hu, X. Nanohole-Boosted Electron Transport between Nanomaterials and Bacteria as a Concept for Nano−Bio Interactions. *Nat. Commun.* **2021**, *12* (1), No. 493.
(30) Xu, S.; Zheng, H.; Ma, R.; Wu, D.; Pan, Y.; Yin, C.; Gao, M.; Wang, W.; Li, W.; Liu, S.; Chai, Z.; Li, R. Vacancies on 2D Transition Metal Dichalcogenides Elicit Ferroptotic Cell Death. *Nat. Commun.* **2020**, *11* (1), No. 3484.
(31) Macrae, C. F.; Edgington, P. R.; McCabe, P.; Pidcock, E.; Shields, G. P.; Taylor, R.; Towler, M.; van De Streek, J. Mercury: Visualization and Analysis of Crystal Structures. *J. Appl. Crystallogr.* **2006**, *39*, 453−457.
(32) Pettersen, E. F.; Goddard, T. D.; Huang, C. C.; Couch, G. S.; Greenblatt, D. M.; Meng, E. C.; Ferrin, T. E. UCSF Chimera—A Visualization System for Exploratory Research and Analysis. *J. Comput. Chem.* **2004**, *25* (13), 1605−1612.
(33) Martínez, L.; Andrade, R.; Birgin, E. G.; Martínez, J. M. PACKMOL: A package for building initial configurations for molecular dynamics simulations. *J. Comput. Chem.* **2009**, *30* (13), 2157−2164.
(34) Van Der Spoel, D.; Lindahl, E.; Hess, B.; Groenhof, G.; Mark, A. E.; Berendsen, H. J. C. GROMACS: Fast, Flexible, and Free. *J. Comput. Chem.* **2005**, *26* (16), 1701−1718.
(35) Wang, Z.; von dem Bussche, A.; Qiu, Y.; Valentin, T. M.; Gion, K.; Kane, A. B.; Hurt, R. H. Chemical Dissolution Pathways of MoS_2 Nanosheets in Biological and Environmental Media. *Environ. Sci. Technol.* **2016**, *50* (13), 7208−7217.
(36) Chen, S.; Shi, N.; Huang, M.; Tan, X.; Yan, X.; Wang, A.; Huang, Y.; Ji, R.; Zhou, D.; Zhu, Y.-G.; Keller, A. A.; Gardea-Torresdey, J. L.; White, J. C.; Zhao, L. MoS_2 Nanosheets−Cyanobacteria Interaction: Reprogrammed Carbon and Nitrogen Metabolism. *ACS Nano* **2021**, *15* (10), 16344−16356.
(37) Philippe, A.; Schaumann, G. E. Interactions of Dissolved Organic Matter with Natural and Engineered Inorganic Colloids: A Review. *Environ. Sci. Technol.* **2014**, *48* (16), 8946−8962.
(38) Herd, H.; Daum, N.; Jones, A. T.; Huwer, H.; Ghandehari, H.; Lehr, C.-M. Nanoparticle Geometry and Surface Orientation Influence Mode of Cellular Uptake. *ACS Nano* **2013**, *7* (3), 1961−1973.
(39) Saikia, J.; Yazdimamaghani, M.; Hadipour Moghaddam, S. P.; Ghandehari, H. Differential Protein Adsorption and Cellular Uptake of Silica Nanoparticles Based on Size and Porosity. *ACS Appl. Mater. Interfaces* **2016**, *8* (50), 34820−34832.
(40) Wang, L. H.; Rothberg, K. G.; Anderson, R. G. Mis-Assembly of Clathrin Lattices on Endosomes Reveals a Regulatory Switch for Coated Pit Formation. *J. Cell Bio.* **1993**, *123* (5), 1107−1117.
(41) Rodal, S. K.; Skretting, G.; Garred, O.; Vilhardt, F.; van Deurs, B.; Sandvig, K. Extraction of Cholesterol with Methyl-Beta-Cyclodextrin Perturbs Formation of Clathrin-Coated Endocytic Vesicles. *Mol. Biol. Cell* **1999**, *10* (4), 961−974.
(42) Jiang, X.; Röcker, C.; Hafner, M.; Brandholt, S.; Dörlich, R. M.; Nienhaus, G. U. Endo- and Exocytosis of Zwitterionic Quantum Dot Nanoparticles by Live HeLa Cells. *ACS Nano* **2010**, *4* (11), 6787−6797.
(43) Yuan, P.; Zhou, Q.; Hu, X. The Phases of WS_2 Nanosheets Influence Uptake, Oxidative Stress, Lipid Peroxidation, Membrane Damage, and Metabolism in Algae. *Environ. Sci. Technol.* **2018**, *52* (22), 13543−13552.
(44) Zou, W.; Zhou, Q.; Zhang, X.; Hu, X. Dissolved Oxygen and Visible Light Irradiation Drive the Structural Alterations and Phytotoxicity Mitigation of Single-Layer Molybdenum Disulfide. *Environ. Sci. Technol.* **2019**, *53* (13), 7759−7769.
(45) Saftig, P.; Klumperman, J. Lysosome Biogenesis and Lysosomal Membrane Proteins: Trafficking Meets Function. *Nat. Rev. Mol. Cell Biol.* **2009**, *10* (9), 623−635.
(46) George, S.; Lin, S.; Ji, Z.; Thomas, C. R.; Li, L.; Mecklenburg, M.; Meng, H.; Wang, X.; Zhang, H.; Xia, T.; Hohman, J. N.; Lin, S.; Zink, J. I.; Weiss, P. S.; Nel, A. E. Surface Defects on Plate-Shaped Silver Nanoparticles Contribute to Its Hazard Potential in a Fish Gill Cell Line and Zebrafish Embryos. *ACS Nano* **2012**, *6* (5), 3745−3759.
(47) Shoji, K.; Ohashi, K.; Sampei, K.; Oikawa, M.; Mizuno, K. Cytochalasin D Acts as an Inhibitor of the Actin−Cofilin Interaction. *Biochem. Biophys. Res. Co.* **2012**, *424* (1), 52−57.
(48) Hsu, C. Y. M.; Uludağ, H. Cellular Uptake Pathways of Lipid-Modified Cationic Polymers in Gene Delivery to Primary Cells. *Biomaterials* **2012**, *33* (31), 7834−7848.
(49) Nabi, I. R.; Le, P. U. Caveolae/Raft-Dependent Endocytosis. *J. Cell Bio.* **2003**, *161* (4), 673−677.
(50) Zhao, J.; Stenzel, M. H. Entry of Nanoparticles into Cells: The Importance of Nanoparticle Properties. *Polym. Chem.* **2018**, *9* (3), 259−272.
(51) Christofides, K.; Menon, R.; Jones, C. E. Endocytosis of G Protein-Coupled Receptors and Their Ligands: Is There a Role in Metal Trafficking? *Cell Biochem. Biophys.* **2018**, *76* (3), 329−337.
(52) Muoth, C.; Rottmar, M.; Schipanski, A.; Gmuender, C.; Maniura-Weber, K.; Wick, P.; Buerki-Thurnherr, T. A Micropatterning Approach to Study the Influence of Actin Cytoskeletal Organization on Polystyrene Nanoparticle Uptake by BeWo Cells. *RSC Adv.* **2016**, *6* (76), 72827−72835.
(53) Palanivel, R.; Ganguly, R.; Turdi, S.; Xu, A.; Sweeney, G. Adiponectin Stimulates Rho-Mediated Actin Cytoskeleton Remodeling and Glucose Uptake via APPL1 in Primary Cardiomyocytes. *Metabolism* **2014**, *63* (10), 1363−1373.
(54) Fortin, C.; Campbell, P. G. C. Silver Uptake by the Green Alga *Chlamydomonas reinhardtii* in Relation to Chemical Speciation: Influence of Chloride. *Environ. Toxicol. Chem.* **2000**, *19* (11), 2769−2778.
(55) Zou, W.; Zhao, C.; Zhang, X.; Jin, C.; Jiang, K.; Zhou, Q. Mitigation Effects and Associated Mechanisms of Environmentally Relevant Thiols on the Phytotoxicity of Molybdenum Disulfide Nanosheets. *Environ. Sci. Technol.* **2022**, *56* (13), 9556−9568.
(56) Sun, K.; Song, Y.; Liu, Z.; Jing, M.; Wan, J.; Tang, J.; Liu, R. Toxicity Assessment of Fluoranthene, Benz(a)Anthracene and Its Mixed Pollution in Soil: Studies at the Molecular and Animal Levels. *Ecotox. Environ. Safe.* **2020**, *202*, No. 110864.
(57) Zeinabad, H. A.; Kachooei, E.; Saboury, A. A.; Kostova, I.; Attar, F.; Vaezzadeh, M.; Falahati, M. Thermodynamic and Conformational Changes of Protein toward Interaction with Nanoparticles: A Spectroscopic Overview. *RSC Adv.* **2016**, *6* (107), 105903−105919.
(58) Sun, K.; White, J. C.; Qiu, H.; van Gestel, C. A. M.; Peijnenburg, W. J. G. M.; He, E. Coupled Lipidomics and Digital Pathology as an Effective Strategy to Identify Novel Adverse Outcome Pathways in *Eisenia fetida* Exposed to MoS_2 Nanosheets and Ionic Mo. *Environ. Sci. Technol.* **2023**, *57* (30), 11009−11021.
(59) Dale, C. T. Signal Transduction by the Wnt Family of Ligands. *Biochem. J.* **1998**, *329* (Pt 2), 209−223.
(60) Kettler, K.; Veltman, K.; van de Meent, D.; van Wezel, A.; Hendriks, A. J. Cellular Uptake of Nanoparticles as Determined by Particle Properties, Experimental Conditions, and Cell Type. *Environ. Toxicol. Chem.* **2014**, *33* (3), 481−492.
(61) Li, X.; Qiu, H.; Zhang, P.; Song, L.; Romero-Freire, A.; He, E. Role of Heteroaggregation and Internalization in the Toxicity of Differently Sized and Charged Plastic Nanoparticles to Freshwater Microalgae. *Environ. Pollut.* **2023**, *316*, No. 120517.

https://doi.org/10.1021/acs.est.3c06665
Environ. Sci. Technol. 2023, 57, 21637−21649